UCRL-TR-213040

LAWRENCE
LIVERMORE
NATIONAL
LABORATORY

Preliminary Report on the Feasibility of Using Synthetic Aperture Radar Interferometry to Image Localized Strain as a Discriminator of Geothermal Resources

W. Foxall

June 20, 2005

Disclaimer

This work was performed under the auspices of the U.S. Department of Energy by University of California, Lawrence Livermore National Laboratory under Contract W-7405-Eng-48.

UCRL-TR-213040

PRELIMINARY REPORT ON THE FEASIBILITY OF USING SYNTHETIC APERTURE RADAR INTERFEROMETRY TO IMAGE LOCALIZED STRAIN AS A DISCRIMINATOR OF GEOTHERMAL RESOURCES

Bill Foxall
Lawrence Livermore National Laboratory

June 20, 2005

INTRODUCTION

Most producing geothermal fields and known geothermal resources in the Basin and Range province are associated with Quaternary active fault systems, within which hydrothermal fluids are presumed to circulate from depth to relatively shallow production levels through high permeability fractures. Research at the Dixie Valley field by Barton et al. (1997) indicates that hydraulically conductive fractures within the Stillwater fault zone are those that have orientations such that the fractures are critically stressed for normal shear failure under the regional tectonic stress field. In general, therefore, we might expect geothermal resources to occur in areas of high inter-seismic strain accumulation, and where faults are favorably oriented with respect to the regional strain tensor; in the case of Basin and Range normal faults, these would generally be faults striking normal to the direction of maximum extension. Expanding this hypothesis, Blewitt et al. (2003), based on preliminary, broad-scale analysis of regional strain and average fault strike in the northwestern Basin and Range, have proposed that geothermal resources occur in areas where fault-normal extension associated with shear strain is the greatest.

Caskey and Wesnousky (2000) presented evidence that the Dixie Valley field occupies a 10 km-long gap between prehistoric Holocene ruptures of the fault segments on either side. Modeled maximum shear and Coulomb failure stress are high within the gap owing to the stress concentrations at the ends of the ruptures. These results suggest that a major contributing factor to the enhanced permeability at fault-hosted geothermal systems may be localized stress and strain concentrations within fault zone segments. This notion is generally consistent with the common occurrence of geothermal fields within fault offsets (pull-aparts) along strike-slip fault systems, where the local strain field has a large extensional component (e.g., Salton Sea and Coso). Blewitt et al. (2003) suggested that resources correlate with abrupt changes in fault orientation and with changes in the direction of extensional strain.

On a regional scale, most of the known economic geothermal resources, and particularly producing fields, in western Nevada are located within or at the margins of two belts of concentrated strain and seismicity, the Central Nevada Seismic Zone and the

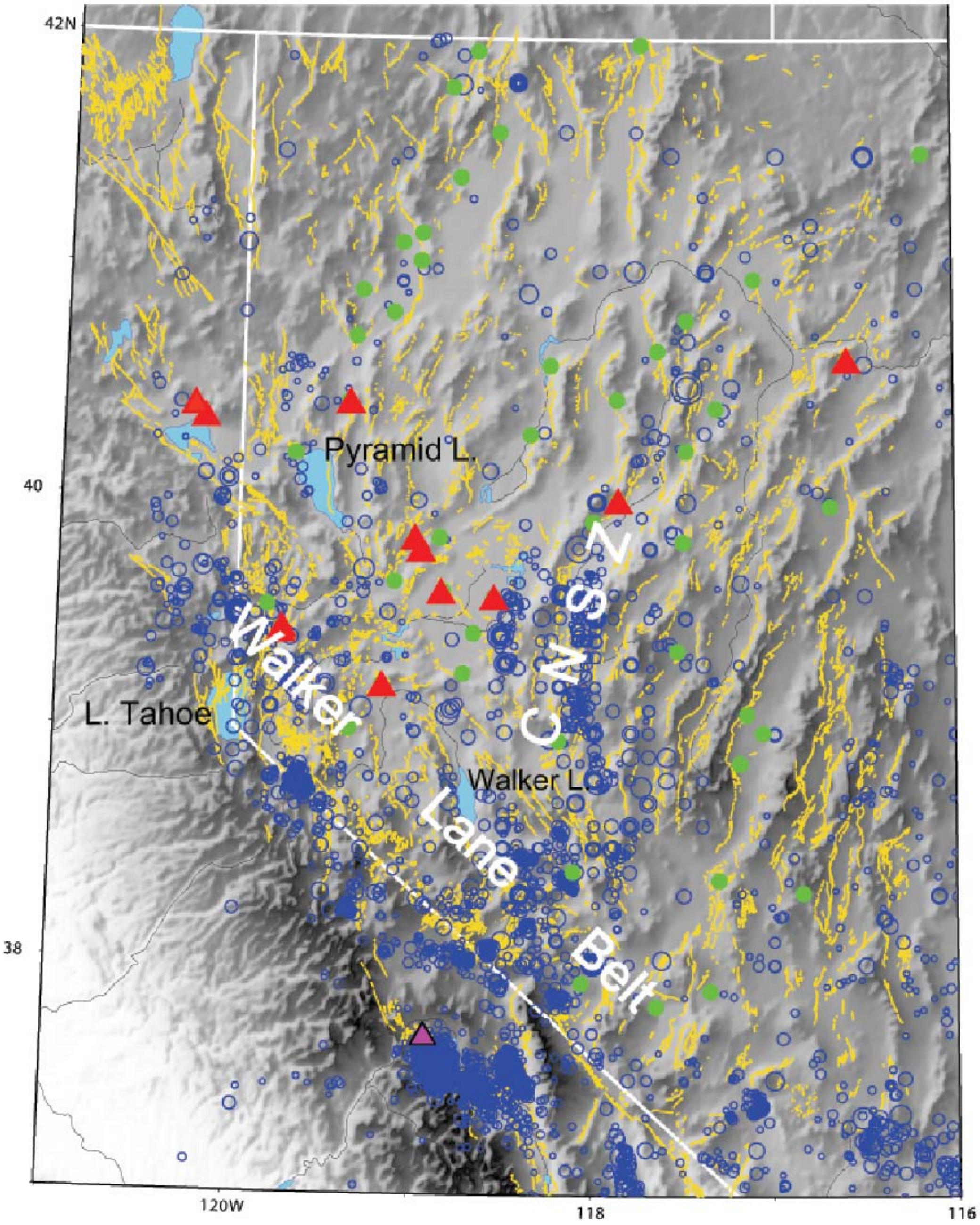

Figure 1: Map of northwestern Nevada and eastern California showing earthquakes M>3 (blue), Quaternary-active faults (USGS, 2004) (yellow), geothermal power plants (red) and wells with temperature >100°C (Great Basin Center, 2005) (green)

Walker Lane belt (Figure 1). Resources northeast of the northern Walker Lane belt and most of the wells having temperatures greater than 100°C are located within the broad Humbolt structural zone of north northeast- to northeast-striking left-lateral and normal faults and other relatively narrow northeast-trending belts (Faulds et al., 2004; Blewitt et al., 2003).

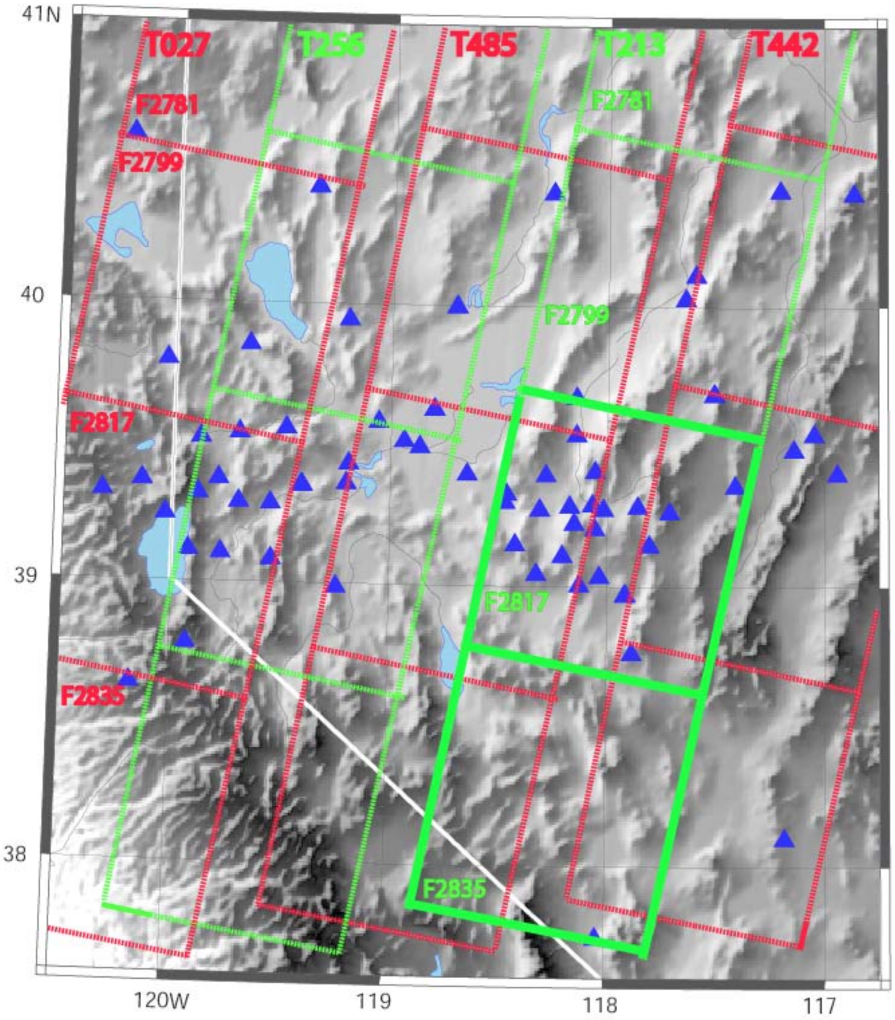

Figure 2: Northwestern Nevada GPS monument locations (blue triangles) and ERS-1/2 descending orbit coverage (green and red frames). Satellite track and frame denoted by **T** and **F**, respectively. Track 213, Frames 2817 and 2835 shown highlighted in green.

Geodetic measurements, seismicity, geology, and remote sensing can be used to investigate whether localized perturbations in the magnitude and orientation of the regional strain field are systematically associated with fault-hosted hydrothermal systems. Blewitt et al. (2003) mapped the regional horizontal strain field across the Basin and Range by interpolating existing data from the Global Positioning System (GPS) network.

The resolution of the strain map in any particular area is roughly equal to the GPS station spacing, which, apart from repeat campaign surveys of geodetic monuments established along Highway 50 (Hammond and Thatcher, 2004), is several tens to ~100 km (Figure 2). Even though UNR has greatly improved the station coverage by establishing some 60 new sites since the beginning of 2004, the GPS network can provide only the regional-scale strain field within which strain localization can be analyzed. Blewitt et al. (2003) are investigating basin-scale strain concentrations by identifying target areas on the regional strain map, and then deploying relatively dense local GPS arrays with station spacing on the order of 10 km.

Over the past decade repeat-orbit differential synthetic aperture radar interferometry (InSAR) has been used to image ground deformation from a variety of sources. The objective of our research is to evaluate the utility of InSAR in regional reconnaissance for geothermal resources by investigating its ability to image localized strain anomalies. An overview of the InSAR method is given in the Appendix. In contrast with GPS and other ground-based geodetic techniques, InSAR has the unique capability of providing an essentially continuous image of ground surface deformation at a spatial resolution of ~10m – 100m at a regional scale, each individual image covering an area of about 120x120 km. The limitations of InSAR are that it cannot resolve individual horizontal and vertical components of ground displacement, and that unfavorable ground surface conditions, such as steep terrain and vegetation, can cause severe image degradation

The majority of InSAR studies to date have used synthetic aperture radar (SAR) data from the European Space Agency (ESA) ERS-1 and ERS-2 satellites, from which a large data archive covering the period from 1992 until the present is available. Most of the studies have dealt with sources such as earthquakes, petroleum and geothermal production and groundwater extraction that typically generate ground displacements of 1 to 10 cm or greater. Under more or less favorable observing conditions relatively large displacements such as these are readily measurable by InSAR. Several studies have imaged displacements occurring at rates ~1 cm/yr associated with post- or inter-seismic strain accumulation across, for example, the San Andreas (e.g. Lyons and Sandwell, 2003) and North Anatolia (Wright et al., 2001) fault zones. Measuring the ~1 mm inter-seismic displacements that accumulate over time intervals of several years across the western Basin and Range and the Eastern California Shear Zone (ECSZ), however, approaches the signal-to-noise (SNR) limits of current InSAR capabilities. For example, GPS estimates of the strain rate across the northwestern Basin and Range translate to a displacement rate of approximately 6-12 mm/yr over a distance of about 210 km, or about 3-6 mm/yr over the width of an InSAR scene. Since we expect that all or most of this strain will be localized on a few active faults, our goal is to measure displacement rates on the order of 1 mm/yr or less over ~1-10 km baselines crossing the faults, comparable with the precision achieved by GPS.

Peltzer et al. (2001) were able to image a displacement rate of about 3 mm/yr over a distance of 140 km across the ECSZ in the southwestern Mojave desert, and resolved a 1.5 mm/yr discontinuity in the displacement rate across a short section of one active fault. Pelzer et al. estimated that they reduced the noise level in their interferogram from ~5 mm/yr to ~0.5 mm/yr by deriving precise interferometric baselines and by stacking 25 individual interferograms (see Appendix). Our challenge is to achieve comparable precision in the western Basin and Range, where more the rugged topography, forested ranges and ubiquitous occurrence of alkali flats in the intervening basins provide somewhat less favorable conditions than the more subdued topography of the southwestern Mojave desert.

In this report we make an initial evaluation of the capability of InSAR to image cumulative surface displacements in the northwestern Basin and Range over time periods of up to eight years. This evaluation is based on comparison of displacement rates derived from InSAR with ground truth provided by GPS rates along two profiles ranging in length from 60 to 95 km. We find that the spatially averaged InSAR rates along the profiles are generally in good agreement with the GPS rates, although there is considerable scatter in the data. The results of this preliminary analysis suggest that InSAR is capable of measuring displacement rates of a mm/yr (or perhaps even less) where the terrain and ground surface conditions are favorable.

Tectonic Strain Accumulation in the Basin and Range

Recent GPS surveys show that crustal deformation is strongly concentrated within the western 200 km of the Basin and Range province and to a lesser degree across the Wasatch front at its eastern boundary, with little deformation in the intervening 500 km (Bennett et al., 1998; Thatcher et al., 1999; Hammond and Thatcher, 2004). The western zone of deformation coincides with the Walker Lane belt (WLB) and the Central Nevada Seismic Zone (CNSZ), two intersecting belts of concentrated seismic activity and faulting (Figure 1). The WLB follows the eastern front of the Sierra Nevada and is the northwestward continuation of the ECSZ. The ECSZ-WLB accounts for 20-25% of the right-lateral motion between the Pacific and North American plates. The CNSZ trends roughly south-southwest from Pleasant Valley to intersect the WLB north of Mammoth, and is defined by a series of six moderate to large (M>6.5) earthquakes during the 20th century.

Hammond and Thatcher (2004) measured horizontal displacement rates (velocities) across the CNSZ and northern WLB using repeat campaign-mode GPS surveys of monuments installed along Highway 50. Svarc et al. (2002) analyzed data from the Highway 50 array and two other geodetic networks that provide wider north-south coverage of the CNSZ and northern WLB (Figures 2 and 3). The eastern boundary of the CNSZ at about 117.5°W marks the abrupt increase in the strain rate moving from east to west and the beginning of progressive clockwise rotation of the velocity vectors from east-west to northwest. Along the Highway 50 transect, relative motion between the CNSZ at 118°W and the western edge of the WLB near the Sierra Nevada frontal fault zone at 120°W is about 10-11 mm/yr, of which approximately 6 mm/yr is taken up across the WLB west of 119°W.

Velocities across the CNSZ are consistent with right-lateral simple shear and fault-normal extension on a fault striking N10°E (Hammond and Thatcher, 2004; Svarc et al., 2002), which match the right-lateral oblique normal fault offsets observed after the 1954 Fairview Peak-Dixie Valley earthquake sequence. The GPS data permit current strain accumulation to be concentrated in an ~10 km-wide zone centered on the 1954 ruptures, but the resolution is insufficient to conclude this definitively (Svarc et al., 2002). Within the northern WLB seismicity indicates that deformation is distributed among several faults of different types, and the situation is more complex. In addition to right-lateral oblique faults like the Pyramid Lake fault (Briggs and Wesnousky, 2004) that strike northwest parallel to the trend of the WLB, seismicity is associated with both northeast-striking left-lateral oblique faults (e.g. the Olighouse fault and the Carson lineament) and northerly-striking normal faults (e.g. the Genoa fault), some of which show evidence for large historic and pre-historic earthquakes. Svarc et al. (2002) treated the area west of the CNSZ between 118.5°W and the Sierra front at 120.3° as a single northern WL zone, within which the strain field is approximately uniform and can be described by right-lateral simple shear and fault-normal extension on a fault striking N35°W. However, they emphasize that north- and northeast-striking faults are also likely to play an important role. Hammond and Thatcher (2004) split the area into two zones, the northern WLB (118.4°W-119.3°W) and the transition from the WLB to the Sierra Nevada frontal fault zone (119.3°W-120.5°W). They concluded that strain within the northern WLB could not be explained simply by right-lateral shear with normal extension on N35°W-striking faults, but, like Svarc et al., suggest that it also involves north- and northeast-striking faults. Similarly, strain within the westernmost transition zone can be described adequately by right-lateral shear plus normal extension on both N35°W- and north-striking faults. The direction of the maximum (extensional) principal stress is rotated counterclockwise from its direction further east, consistent with the change in strike of normal faults near the Sierra Nevada frontal fault zone. Hammond and Thatcher stress that the strain solution is not unique, indicating the complex partitioning of deformation among the different styles of faulting within the WLB and Sierra Nevada frontal fault zone.

Synthetic Aperture Radar Data Analysis

ERS-1/2 descending (see Appendix) orbit coverage of the CNSZ and northern WLB is shown in Figure 2. We selected Frames 2817 and 2835 of Track 213 for this initial study, and acquired raw data from 34 orbits. The rational for selecting these frames is that the numerous campaign-mode GPS sites, including monuments of the Highway 50 transect, located in Frame 2817 (Figure 3) provide ground-truth measurements against which to calibrate the InSAR results, and that the two frames cover the southern part of the CNSZ and its intersection with the central WLB. The undeveloped Fish Lake geothermal field is in the SE corner of Frame 2835. We produced 33 interferograms for each of the frames from the orbit pairs shown in Figure 4. The interferogram pairs span time intervals (temporal baselines) ranging from 1 to 8.3 years during the period 1992-2000, and have perpendicular baselines (see Appendix) less than 95 m (all but one have baselines less than 65 m). We used a 90m-resolution digital elevation model (DEM) produced by the NASA Shuttle Radar Topography Mission (SRTM) to remove the

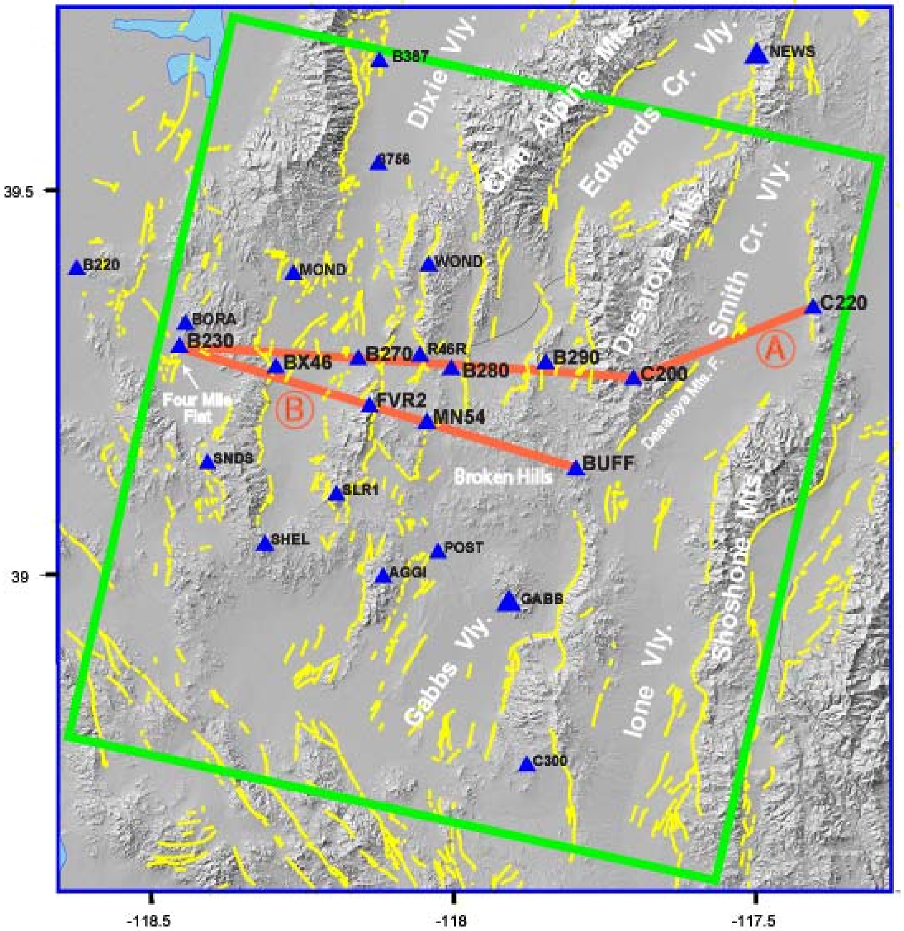

Figure 3: GPS monuments (blue) within ERS Frame 2817, Track 213 (green). Quaternary-active faults shown in yellow. GPS and InSAR profile lines shown in orange; **A** and **B** are Highway 50 (B230-C220) and B230-BUFF profiles, respectively.

topographic contribution from the aligned and flattened interferograms. Phase unwrapping was accomplished using a minimum cost flow algorithm. We examined the individual interferograms and rejected five that were obviously noisy because of snow cover, geometrical decorrelation, or other reasons. We then created stacks using various combinations of the remaining 28 interferograms, as described below.

Results

This section focuses calibration of the results for Frame 2817 against GPS ground truth data. An interferogram stack for Frame 2835 is shown in Figure 5, but is not discussed further in this report. In this and subsequent images, slant range change rate is displayed in color and is superimposed upon the backscatter intensity (brightness). Figure 6 shows the stack of all 28 differential interferograms for Frame 2817. Range change rates are computed relative to a reference resolution element located at approximately 39.0°N 118.3°W. Figure 7 shows a stack of 20 interferograms selected to minimize the number of pairs having a common scene, thus minimizing artifacts stemming from atmospheric path delays in those scenes, and some winter scenes in which snow may cover some of the area. Average range change rates in these stacks are assigned only to those elements for which a minimum of 80% of the interferograms (22 and 16 for the 28- and 20-interferogram stacks, respectively) have valid phase change values. Elements not meeting this requirement - usually in areas of poor phase coherence – are assigned a null (zero) value. Areas of generally low phase coherence are masked out and appear gray in Figures 6 and 7. In general,

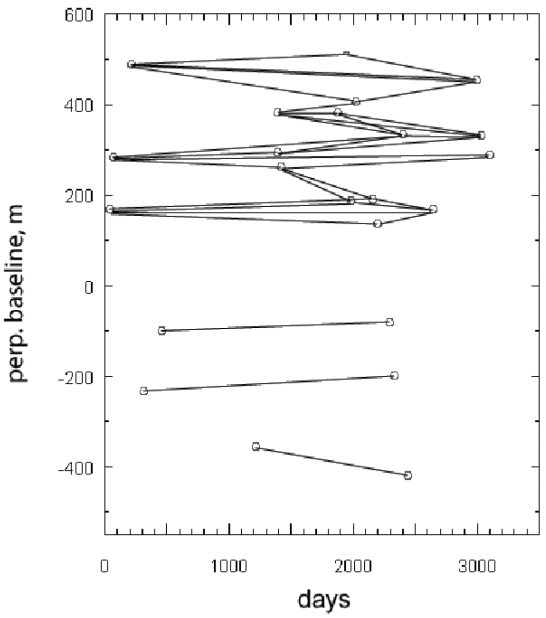

Figure 4: Interferogram orbit pairs.

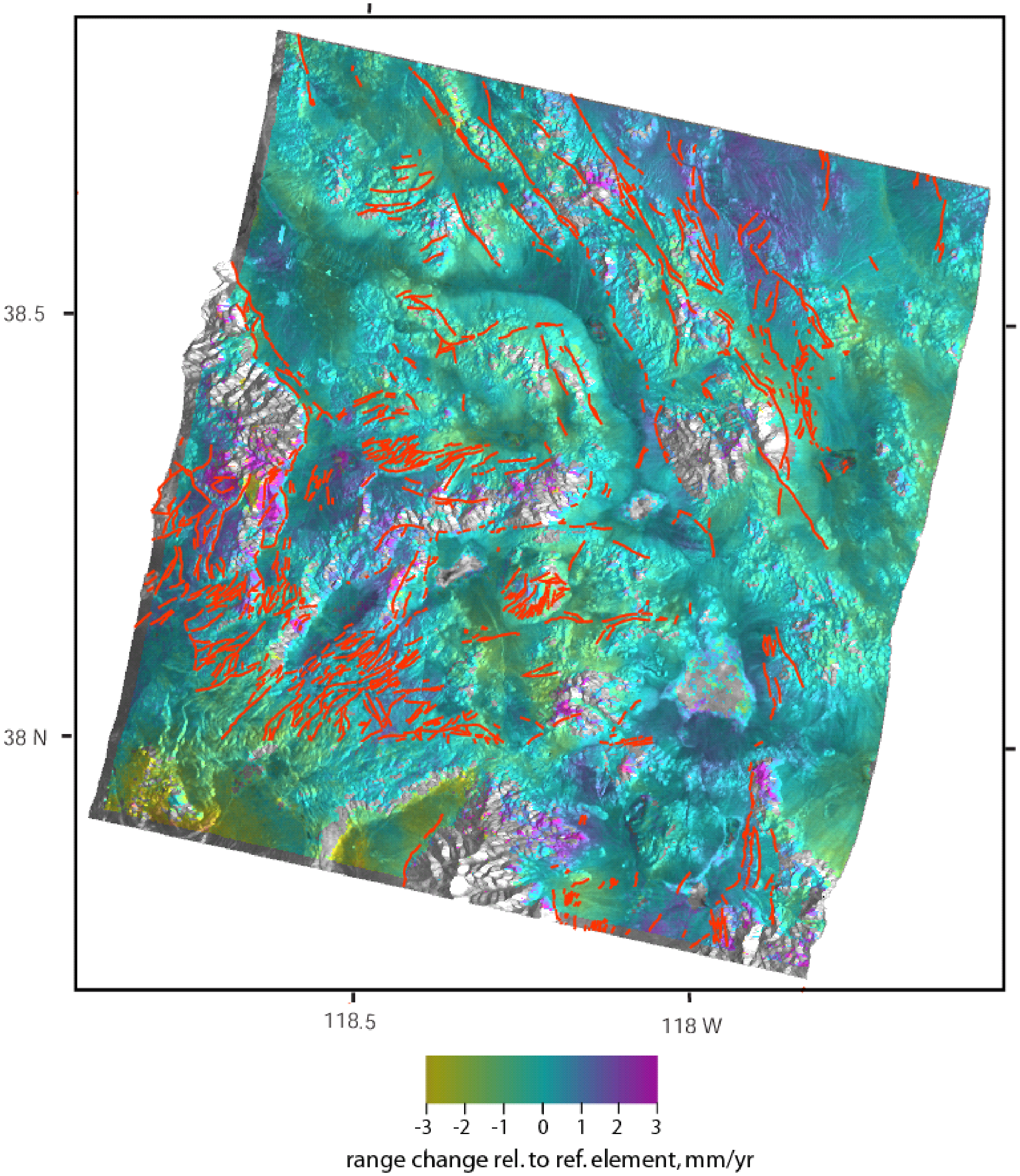

Figure 5: Track 213, Frame 2835 20-interferogram stack covering the period 1992-2000. Range-change rate (color) overlays backscatter intensity (brightness). Quaternary-active faults shown in red.

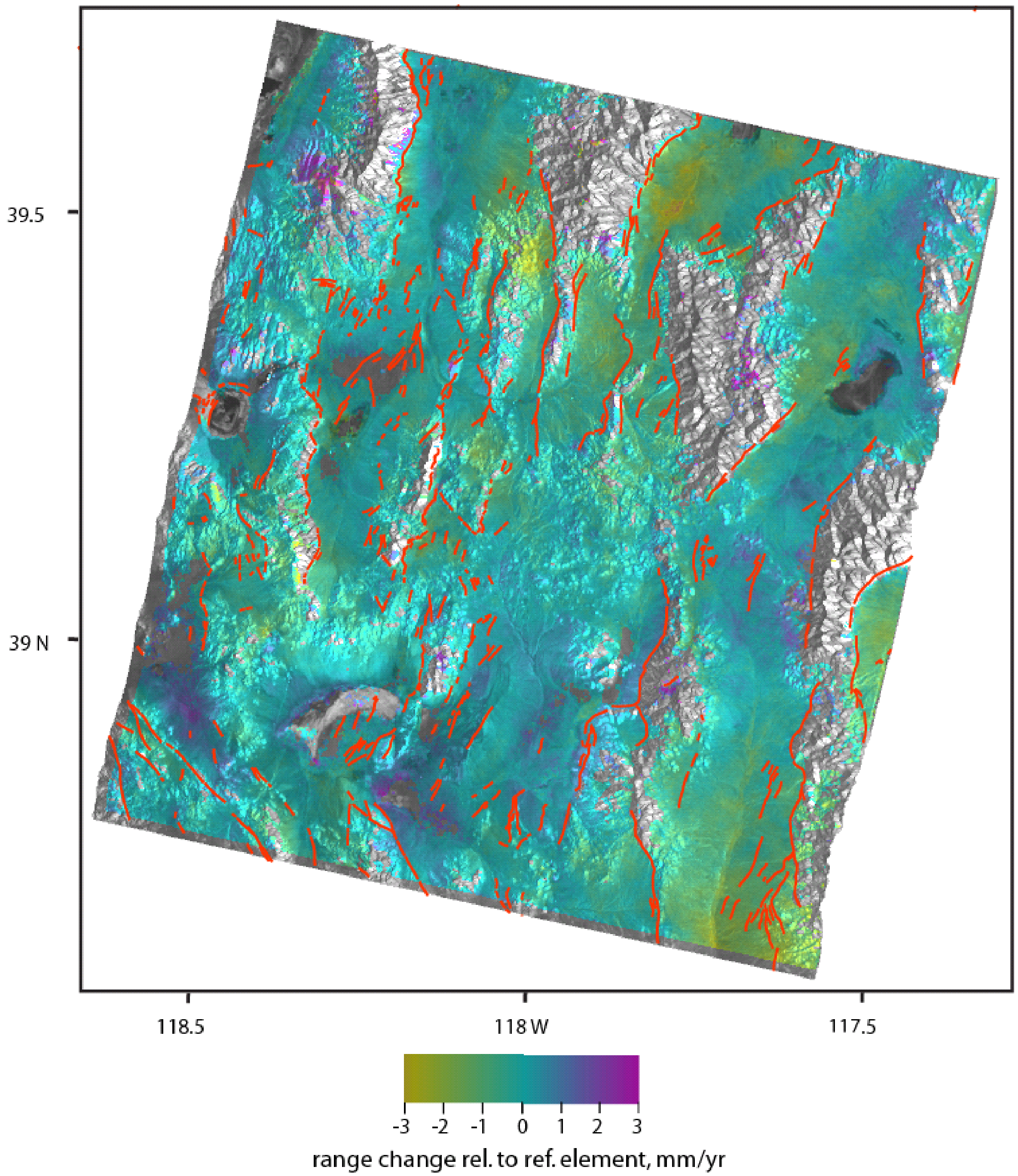

Figure 6: Track 213, Frame 2817 28-interferogram stack covering the period 1992-2000. See Figure 5 for explanation.

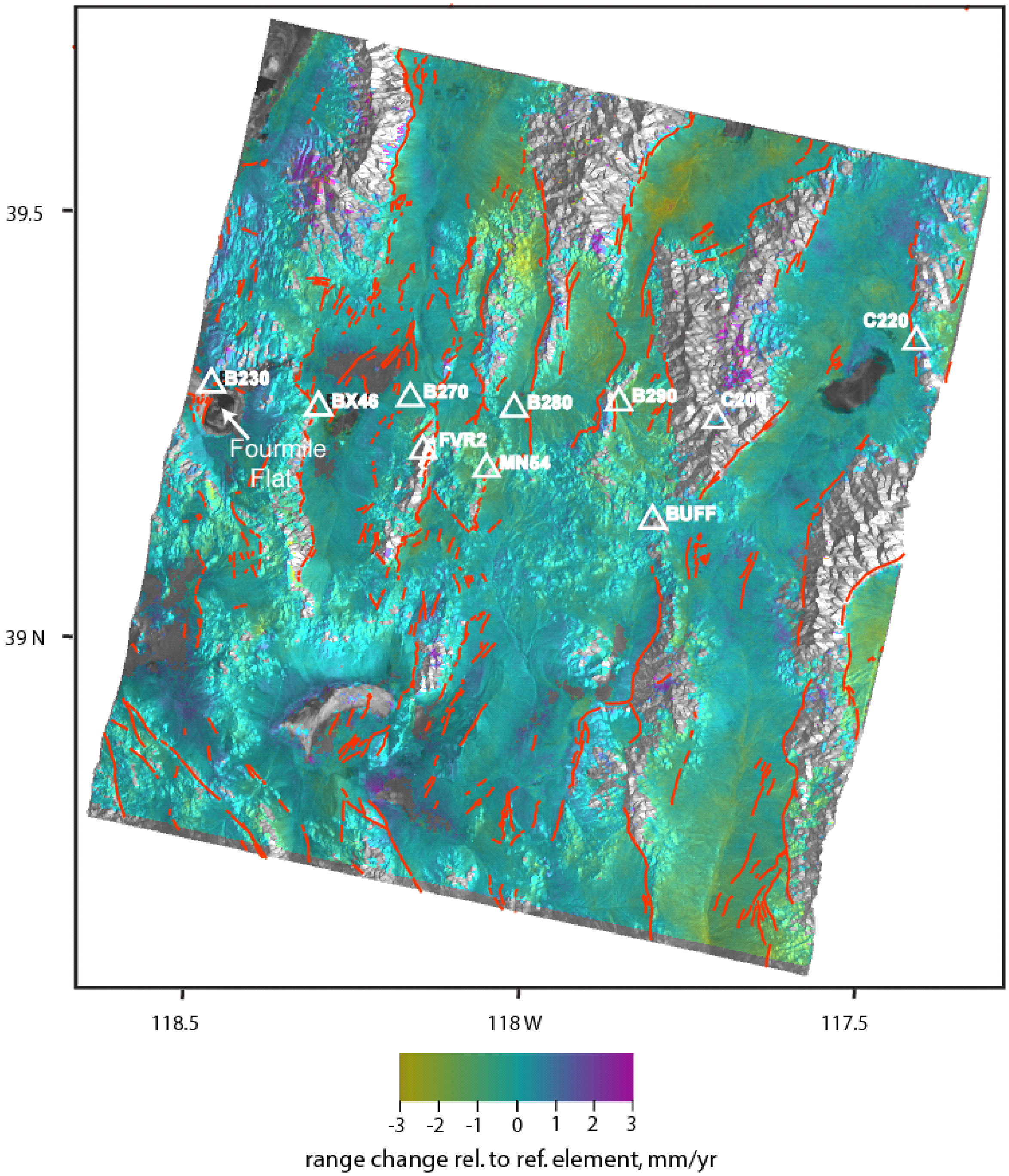

Figure 7: Track 213, Frame 2817 20-interferogram stack covering the period 1992-2000. See Figure 5 for explanation. White triangles are GPS monuments along the Highway 50 and B230-BUFF profiles (Figure 3).

coherence is lost over the ranges and over the alkali flats (e.g. Fourmile Flat, Figure 7) located in many of the basins. Decorrelation over the ranges is caused by vegetation in addition to geometrical decorrelation, layover and shadowing, while changes in water content causes decorrelation over the alkali flats.

The 28- and 20-interferogram stacks are closely similar, indicating that the result is robust with respect to the subset of interferograms selected and that stacking achieves the desired effect of suppressing spurious noise in individual interferograms. There is an overall trend to negative range change rate from west to east. However, the apparent range change rates are subtle, less than 2 mm/yr across the entire width of the frame, so it is difficult to distinguish true signals from noise. To evaluate whether the apparent range changes do, in fact, correspond to ground deformation, we compared the range change values along the two profiles shown in Figure 3 with available GPS data. The first profile follows the Highway 50 array of Hammond and Thatcher (2004) between monuments B230 and C200, and C200 and C220. The second profile is through five monuments between B230 and BUFF that form part of the GPS network analyzed by Svarc et al. (2002).

Figures 8 and 9 compare the Highway 50 and B230-BUFF GPS profiles, respectively, with the range change rates from the 20-interferogram stack. GPS horizontal displacement rates relative to stable North America are converted to range change rates, v_r, using:

$$v_r = -(v_e \cos\lambda + v_n \sin\lambda)\sin\theta \qquad (1)$$

where v_e and v_n are the east and north components of the GPS rate, respectively, λ is the satellite track azimuth (192°) and θ the average radar look angle across the scene (23°). The GPS rates are plotted with $\pm 1\sigma$ error bars computed from the standard deviations for rates relative to stable North America given by Hammond and Thatcher (2004) and Svarc et al. (2002).

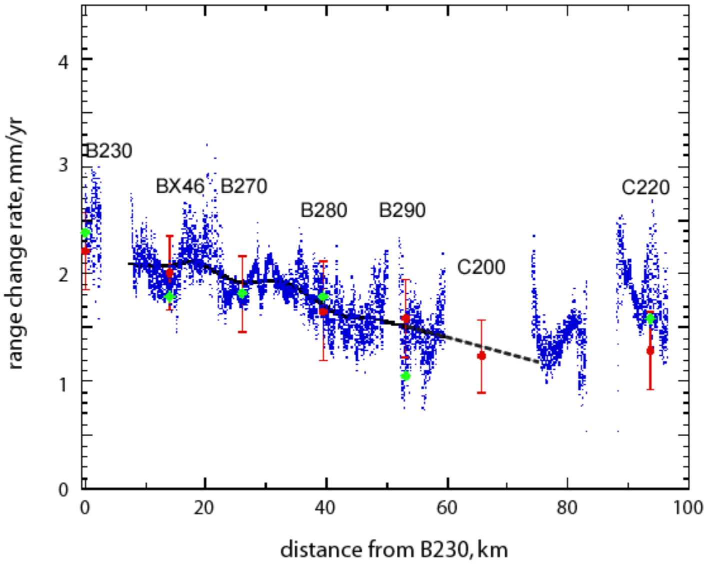

Figure 8: InSAR (blue) and GPS (red) range change rates along the Highway 50 profile (B230-C220, Figure 3). Error bars for GPS rates are ±1σ. Green triangles are point averages of InSAR values for elements centered at the locations of the GPS monuments.

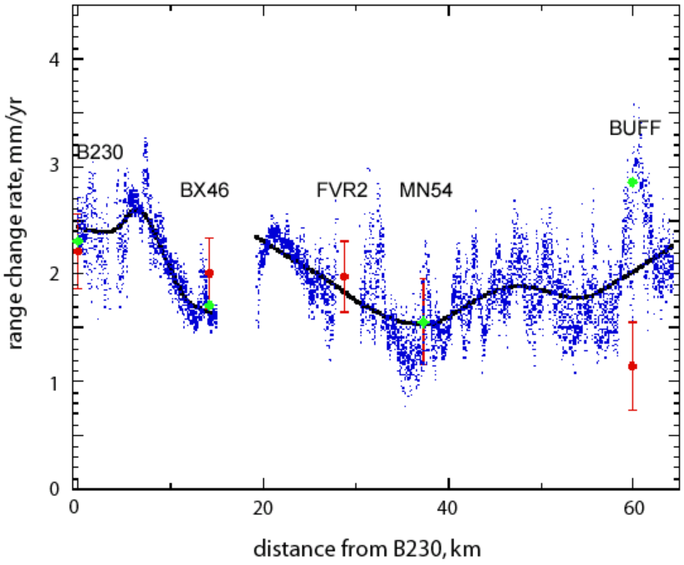

Figure 9: InSAR and GPS range change rates along the B230-BUFF profile (Figure 3). See Figure 8 for explanation.

The overall trends in the InSAR data along the profiles are captured by plotting rates for resolution elements within 0.5 km on either side of the profile line. Gaps in the profiles correspond to low-coherence areas masked out in Figure 7. InSAR rates on the Highway 50 and B230-BUFF profiles are adjusted to match the GPS rates at monuments B270 and MN54, respectively. The black curves are smoothed average fits to the InSAR data. Meaningful curve fits could not be carried out over the first 8 km and last 35 km of the Highway 50 profile because of large data gaps. The average of the InSAR rates of the resolution element coincident with each GPS monument plus the eight neighboring elements is shown by a green diamond. Note that the range change rates computed from the GPS data do not include vertical displacements (Hammond and Thatcher; 2004; Svarc et al., 2002) whereas the InSAR rates include any vertical deformation that may have occurred.

A negative trend in range change rate from west to east is clearly defined in both profiles. The average curve between 10 and 60 km along the Highway 50 profile closely matches the GPS data, which fall within 0.15 mm/yr of the curve. The C200 data point is also within 0.15 mm/yr of the curve extrapolated into the decorrelated region of the Desatoya Mnts. The InSAR point averages at B230, BX46 and B280 are within 0.25 mm/yr of the GPS values. The InSAR point average at B290 falls outside the GPS 1 σ error bar but is poorly determined because B290 is at the edge of narrow area of decorrelation (Figure 7) and some of the interferograms have low coherence in this vicinity. Note, however, that the average curve is close to the GPS rate at this location. The average curve along the first 40 km of B230-BUFF profile also matches the GPS data moderately well, although the curve is not as well constrained because of decorrelation east of BX46 and in the vicinity of FVR2. Point averages at B230 and BX46 fall within the GPS 1 σ error bars.

East of C200 on the Highway 50 profile, the data between 75 and 76 km are consistent with the extrapolated average trend in Figure 8. Further east, however, the trend becomes positive before reversing again at about 89 km. These shorter-wavelength trends are well defined on either side of the area of decorrelation over the alkali flat in Smith Creek Valley. The InSAR point average at C220, which is located within an area of partial decorrelation, is higher than the GPS rate, although still within the 1 σ error.

Extrapolating the apparently well-defined negative trend immediately to the west of C220 would bring it close to the GPS value. The average trend of the B230-BUFF InSAR profile east of MN54 departs significantly from the negative GPS trend. Even allowing for the narrow zone of decorrelation in the vicinity of BUFF, the average curve would still be well outside the GPS 1 σ error.

Discussion

The good fit of the stacked InSAR image to the GPS profiles along most of their lengths suggests that an adequate signal/noise ratio can be achieved through stacking to enable small displacements associated with crustal strain to be measured on a regional scale in areas where the terrain and ground conditions are favorable for interferometry. Using the data scatter (element-to-element variability) within the 1-km swath widths of the profiles as a rough measure of noise suggests that the noise level is approximately 0.1-0.5 mm/yr in areas where ground conditions are favorable, which is generally consistent with the estimate of Peltzer et al. (2001) for stacked data. In less favorable terrain, such as the Broken Hills southwest of the Desatoya Mnts (Figure 3), the noise level is as high as ~1 mm/yr.

Along the two profiles studied, the only major systematic departure of the InSAR from the GPS data occurs along the eastern end of the B230-BUFF profile, which traverses the Broken Hills. Even though the noise level is relatively high, the InSAR rates are systematically above the GPS trend defined by MN54 and BUFF. It seems unlikely that phase unwrapping errors that could cause this kind of bias would have occurred consistently in the processing of all 20 interferograms in the stack. One possible explanation is that the Broken Hills are subsiding, resulting in a net positive range change rate that is not considered in the GPS analysis. Svarc et al. (2001) show a vertical component profile that suggests a broad zone of subsidence east of B230. However, the authors were not confident enough of the relatively noisy vertical data at that time to attach significance to the apparent signal. Hammond (2004) estimated that present uncertainties in vertical GPS velocities are about three times greater than in horizontal velocities, and found vertical motions across the Basin and Range are not resolvably different from zero except close to longitude 114°W.

The profiles illustrate the spatial resolution InSAR achieves compared with the sparse GPS coverage. While the InSAR data in most places match the regional GPS trend, they also exhibit local-scale features at wavelengths on the order of 5-10 km. Since our objective is to investigate strain localization, it is these short-wavelength features, and in particular their relationships to active faults, that are of primary interest to us. Cursory examination of the profiles in the context of the fault map (Figures 3 and 7) suggests possible relationships to active faults. For example, the apparently well defined positive and negative trends between C200 and C220 on the Highway 50 profile might be related to the Desatoya fault, which has mapped Holocene-active segments NE and SW of the main segment that truncates the Desatoya Mnts. on the SE. Features on the Highway 50 profile between B270 and B280 and centered on FVR2 on the B230-BUFF profile might be related to the Fairview fault, which ruptured in 1954. These and features such as the localized negative rate anomaly in Edwards Creek Valley (Figure 7) are the subject of ongoing analysis.

The results also demonstrate one limitation of interferogram stacks: The stacks necessarily include interferograms that span long time intervals in which complete decorrelation occurs over the steep and vegetated ranges. This results in effectively complete loss of data over the ranges, and hence large gaps in the profiles. This is a problem particularly in those parts of the Basin and Range like that covered by Frame 2817, where many of the major active faults are range bounding faults that run along the bases of the steep slopes of the ranges (Figure 3). Therefore, one half of the any displacement signature from such a fault is lost, and has to be inferred by extrapolation from the coherent basins on either side. This might be less of a problem further west and NW within the WLB.

Conclusions and Future Work

The remarkably close fit of stacked InSAR images to GPS data along substantial portions of two profiles indicates that stacking is capable of imaging ground deformation rates accurate to less than a mm/yr in areas where ground conditions are favorable. In the

NW Basin and Range conditions are favorable in the valleys that comprise most of land area, but steep slopes and vegetation result in essentially complete loss of data due to decorrelation over the intervening ranges. Complete decorrelation of more limited extent also occurs over the alkali flats located in many of the valleys.

The results show that interferogram stacks can image rates ~1 mm/yr or less over distances on the order of 100 km, and at a resolution of ~100m. This provides us some confidence that InSAR has the potential for imaging the short-wavelength features - on the order of 1 to 10 km - in the deformation field that we expect to be associated with strain localization and slip on active faults, even at the slow rates that are generally thought to characterize Basin and Range faults. Whether that is in fact proves to be the case depends on how strain across the region is partitioned between the faults (i.e. does most of the North American-Pacific plate motion occur on just a few relatively fast-moving faults?) and at what depth (the locking depth) slip is occurring. We will address these questions in the next phase of the project. We have begun integrating the InSAR images for Frames 2817 and 2835 with fault, GPS and seismicity data sets to enable detailed analysis and evaluation of possible localized strain signatures. We are expanding the study region to cover the northern Walker Lane Belt to the west by acquiring multiple scenes from Tracks 485, 256 and 027 (Figure 2), and will begin stack processing as soon as we receive the data. We are also developing a stacking approach utilizing weighted averaging, rather than the unweighted time averaging employed in conventional interferogram stacks, to further improve signal/noise ratio.

REFERENCES

Bennett, R.A., B.P. Wernicke, and J.L. Davis, Continuous GPS measurements of contemporary deformation across the northern Basin and Range province, Geophys. Res. Let., **25**, 563-566, 1998.

Barton, C.A., S. Hickman, R. Morin, M.D. Zoback, T. Finkbeiner, J. Sass, and D. Benoit, Fracture permeability and its relationship to in-situ stress in the Dixie Valley, Nevada, geothermal reservoir, Proc. 22nd Workshop on Geotherm. Reservoir Eng., Stanford Univ., CA, Jan. 27-29, 1997, SGP-TR-155, 147-152, 1997.

Blewitt, G., M.F. Coolbaugh, D.L. Swatzky, W. Holt, J.L. Davis, and R.A. Bennett, Targeting of potential geothermal resources in the Great Basin from regional to basin-scale relationships between geodetic strain and geological structures, Geotherm. Resources Coun. Trans., **27**, 2003.

Briggs, R.W. and S.G. Wesnousky, Late Pleistocene fault slip rate, earthquake recurrence, and recency of slip along the Pyramid Lake fault zone, northern Walker Lane, United States, Jo. Geophys. Res., **109**, B08402, doi:10.1029/2003JB002717, 2004

Bürgmann, R., P.A. Rosen, and E.J. Fielding, Synthetic aperture radar interferometry to measure Earth's surface topography and its deformation, Ann. Rev. Earth Planet. Sci., **28**, 169-209, 2000.

Caskey, S.J., and S.G. Wesnousky, Active faulting and stress redistributions in the Dixie Valley, Beowawe, and Bradys geothermal fields: Implications for geothermal exploration in the Basin and Range, Proc. 25th Workshop on Geotherm. Reservoir Eng., Stanford Univ., CA, Jan. 24-26, 2000, SGP-TR-165, 9 p, 2000.

Curlander, J.C. and R.N. McDonough, Synthetic aperture radar: Systems and signal processing, John Wiley and Sons, New York, 647 p, 1991.

Faulds, J.E., L.J. Garside, and G.L. Oppliger, Geological and Geophysical Analysis of the Desert Peak-Brady Geothermal Fields: Elucidating Structural Controls on Geothermal Resources in the Great Basin, presentation to the Great Basin Geothermal Workshop, Univ. Nevada, Reno, http://www.unr.edu/geothermal/GBGeothermalMeetingPresentations.htm, Nov. 5, 2004.

Foxall, B., and D. Vasco, Inversion of synthetic aperture radar interferograms for sources of production-related subsidence at the Dixie Valley geothermal field, Proc., 28th Workshop on Geothermal Reservoir Engineering, Stanford University, CA, Jan. 27-29, 2003, SGP-TR-173, 7 p, 2003.

Great Basin Center, Geothermal and exploration spatial data, Univ. Nevada, Reno, http://www.unr.edu/geothermal/datalist.html#Geothermal__Data, 2005.

Hammond, W.C., Vertical motion of the Basin and Range, western United States from 10 Years of Campaign GPS, *in* Cahiers du Centre Européen de Géodynamique et de Séismologie, Proceedings of the workshop: *The State of GPS Vertical Positioning Precision: Separation of Earth Processes by Space Geodesy*, ed T. van Dam, **v 23**, 6 p, 2004.

Hammond, W.C. and W. Thatcher, Contemporary tectonic deformation of the Basin and Range province, western United States: 10 years of observation with the Global Positioning System, Jo. Geophys. Res., **109**, B08403, doi:10.1029/2003JB002746, 2004.

Hanssen, R.F., Radar interferometry: Data interpretation and error analysis, Kluwer Academic Publishers, Dordrecht, 308 p, 2001.

Lyons, S. and D. Sandwell, Fault creep along the southern San Andreas from interferometric synthetic aperture radar, permanent scatterers, and stacking, Jo. Geophys. Res., **108**, B5, 10.1029/2002JB001831, 2003.

Peltzer, G., F. Crampe, S. Hensley, and P. Rosen, Transient strain accumulation and fault interaction in the eastern California shear zone, Geology, **29**, 975-978, 2001.

Rosen, P.A., S. Hensley, I.R. Joughin, F.K. Lee, S.N. Madsen, E. Rodríguez, and R.M. Goldstein, Synthetic aperture radar interferometry, Proc. IEEE, **88**, 333-382, 2000.

Svarc, J.L., J.C. Savage, W.H. Prescott, and A.R. Ramelli, Strain accumulation and rotation in western Nevada, 1993-2000, J. Geophys. Res., **107**, B5, 10.1029/2001JB000579, 2002.

Thatcher, W., G.R. Foulger, B.R. Julian, J. Svarc, E. Quilty, and G.W. Bawden, Present-day deformation across the Basin and Range province, western United States, Science, **283**, 1714-1718, 1999.

U.S. Geological Survey, Quaternary Fault and Fold Database for the United States, http://qfaults.cr.usgs.gov , 2004.

Wright, T., B. Parsons and E. Fielding, Measurement of interseismic strain accumulation across the North Anatolia fault by satellite radar interferometry, Geophys. Res. Let., **28**, 2117-2120, 2001.

APPENDIX

Overview of Synthetic Aperture Radar Interferometry

Overview of Synthetic Aperture Radar Interferometry

This appendix gives a brief overview of differential InSAR. Detailed descriptions of the method and its application to imaging ground surface deformation are given in review articles by Rosen et al. (2000) and Bürgmann et al. (2000), and the book by Hanssen (2001). Figure A1 shows the basic InSAR imaging geometry, where P and P' are nearby positions of the satellite during two different orbits. The SAR antennas mounted on the ERS satellites point to the right perpendicular to the satellite track azimuth and downwards a look angle, θ, of about 23°. This geometry defines an orthogonal “radar” coordinate system in which distances are measured along the track azimuth and along the slant range, R, in the look direction. The radar images a continuous swath of the Earth’s surface about 120 km wide in ground range (Figure A1) during each orbit, which is divided into frames each about 150 km long in the azimuth direction. Data are recorded during both descending (satellite heading north to south) and ascending (south to north) orbits, but by far most of the archived data is from descending orbits. Recorded raw data comprise the full complex signals of radar echos backscattered from the ground surface, from which both amplitudes and phases can be recovered. The complex image (scene) of a frame produced by synthetic aperture processing has resolutions of approximately 25.5 m and 5.5 m in range and azimuth, respectively. A backscatter intensity (brightness) image of the ground surface - similar in appearance to an optical image of topography, cultural features, etc. - is produced by mapping the amplitudes of the resolution elements across the scene.

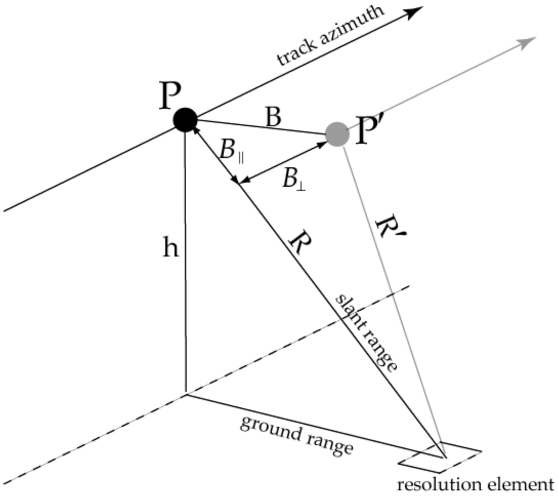

Figure A1: *InSAR imaging geometry*

The basic principle of InSAR is that the difference between the phases of the radar echos received at P and P' from a resolution element on the ground is proportional to the difference in the line of sight path lengths to the two positions. The distance between the satellites is termed the spatial baseline, B, usually given in terms of its components $B_{\|}$ and $B_{\perp}$ parallel and perpendicular to the look vector, respectively. Phase differences, $\psi = \varphi_1 - \varphi_2$, are computed by multiplication of the two complex images:

$$z_1 z_2^* = |z_1| e^{j\phi_1} |z_2| e^{-j\phi_2} = |z_1||z_2| e^{j(\phi_1 - \phi_2)} \qquad \text{(A1)}$$

and mapped across the scene to form an interferogram.

The three main contributions to path differences and hence to the phase differences mapped in the interferogram are: (1) Changes in slant range, $R - R'$, caused by any coherent displacements of the ground surface that occurred during the time interval (the temporal baseline) between the two orbits; (2) differences in slant range that result from viewing the topography from the two slightly different satellite positions; and (3) changes in the refractive index of the atmosphere from scene to scene due to fluctuations in water vapor content that cause variable path delays that look like apparent range changes. The last two contributions must be removed to produce a differential interferogram in which the phase differences are the result of ground displacements alone. The topographic contribution is removed either by subtracting a synthetic interferogram created from a digital elevation model (DEM) or (since Contribution 2 above can be used to generate topographic models from interferograms) by incorporating additional orbit scenes. Sensitivity to topography increases with increasing $B_{\perp}$, so short baselines (ideally substantially less than 100 m) are preferred for differential interferometry. Atmospheric path delays are indistinguishable from ground displacements and cannot be removed from individual interferograms. They can, however, be effectively attenuated by stacking (averaging) multiple interferograms. The stacking process is further described below.

Although phase differences caused by displacements and topography can be arbitrarily large, the radar detects only the principal value of the phase modulo 2π radians. Therefore, a differential interferogram is “wrapped’ into the -π – +π radian interval and appears as a series of interference fringes. In order to recover the true phase the interferogram is “unwrapped”, which essentially involves starting at a reference resolution element of known or assumed displacement and working outwards in all directions adding or subtracting 2π radians for each fringe crossed. Unwrapping in the presence of noise and inevitable data gaps is non-unique and usually the most problematic part of InSAR processing. Several unwrapping schemes are in general use.

The final stages of processing are to convert the unwrapped differential interferogram to a range change map, which is then transformed from radar (range-azimuth) to geographical coordinates. All three components of the ground displacement of each resolution element (relative to the reference element) are projected on to the single (scalar) range change measurement, so that the individual components cannot be resolved. The steep look angle (23°) of the ERS radars means that vertical displacements make proportionally greater contributions to range changes than horizontal displacements. The horizontal component parallel to the satellite track makes zero contribution to range change (see Equation 1). These measurement characteristics contrast with those of GPS, which measures all three displacement components (i.e. absolute 3D position) within an inertial frame (but usually reported relative to a fixed reference point on the Earth’s surface), but for which the vertical displacement precision is significantly less than the horizontal (e.g., Svarc et al., 2002; Hammond, 2004).

Phase noise in interferograms arises from loss of (cross) correlation between the two images, which is the normalized magnitude of the complex product in Equation A1:

$$\gamma = \frac{\left|E\{z_1 z_2^*\}\right|}{\sqrt{E\{|z_1|^2\}E\{|z_2|^2\}}} \qquad 0 \le \gamma \le 1 \qquad \text{(A2)}$$

where $E\{.\}$ denotes expectation value. The correlation is commonly referred to as coherence in InSAR literature. Correlation is related to SNR by:

$$SNR = \frac{\gamma}{1-\gamma} \qquad \text{(A3)}$$

The main sources of phase noise are geometric and temporal decorrelation. Geometric decorrelation is a result of the different incidence angles of the radar beam at a given resolution element due to the separation between the two satellite positions, and is exacerbated by topographic slope. Geometrical decorrelation increases with increasing $B_\perp$ and steeper slopes; for ERS-1/2, complete decorrelation occurs over a flat surface when the $B_\perp$ is about 1.1 km Temporal decorrelation occurs when there is a change between the two scenes in the individual point scatterers within a resolution element, which destroys the coherence of the phases. This occurs when the individual scatters undergo incoherent displacements between the scenes, caused, for example, by vegetation growth or movement in the wind, agricultural activity, changes in ground moisture, or snowfall. Temporal decorrelation naturally is more severe for long temporal baselines.

Because of its inherent non-uniqueness, phase unwrapping is subject to significant random and systematic errors. These are ameliorated by filtering wrapped interferograms to reduce phase noise. The most common form of filtering is simple spatial averaging ("multi-looking") of neighboring resolution elements during and after interferogram formation. More sophisticated adaptive filters can also be used to improve the signal-to-noise ratio (SNR) of the interferogram. Note that filtering in general increases SNR at the expense of spatial resolution. In regions of high relief the oblique viewing geometry causes geometrical distortion of the image in the slant range direction (see Curlander and McDonough, 1991, Chap. 8), which result in loss of either phase information or the entire backscattered signal. Layover occurs when the terrain slopes towards the radar at an angle greater than the incidence angle. This causes the slant range to a mountain peak to be less than to its base, so that the mountain appears to lean towards the radar. Echos from multiple target locations within the layover area are received simultaneously so that phase information is lost. Shadowed areas from which no backscattered signals at all are received occur when the terrain slopes away from the radar at an angle greater than the incidence angle. Layover and shadowing cause gaps or areas of low-correlation in the interferogram that are a major source of unwrapping errors.

As we mentioned above, artifacts caused by atmospheric propagation delays cannot be identified on individual interferograms, but can be dealt with by stacking multiple scenes. Stacking enhances signals that are coherent through the stack and reduces incoherent noise by a factor of $1/\sqrt{N}$, where N is the number of interferograms in the stack. Fluctuations in atmospheric water vapor sufficient to give rise to significant artifacts occur on all spatial scales up to about 10 km but are uncorrelated in time and hence comprise one source of incoherent noise. The conventional stacking approach used in InSAR computes the mean range change *rate* from N unwrapped differential interferograms by dividing the sum of the N range change values at each resolution element by the sum of the temporal baselines. Inherent in this estimate is the assumption that the range change rate (i.e. the deformation rate) is constant over the time interval between the first and last orbits used in the interferograms comprising the stack. This assumption is probably appropriate for most cases of inter-seismic tectonic deformation. Given the assumed constant deformation rate, stacking interferograms can be viewed as combining two operations; extracting very small cumulative displacements from relatively coherent interferograms having short temporal baselines, and extracting larger cumulative displacements from noisier long-baseline interferograms. The unweighted average used in this conventional stacking approach does not take into account the large variations in noise level inherent in combining short- and long-baseline interferograms.